RSC Advances

PAPER

First-principles investigation on dimerization of metal-encapsulated gold nanoclusters

Cite this: *RSC Adv.*, 2014, **4**, 192

Sora Park,[a] Gunn Kim*[b] and Young-Kyun Kwon*[a]

Received 11th October 2013
Accepted 4th November 2013

DOI: 10.1039/c3ra45742g

www.rsc.org/advances

Density functional theory is used to study dimerization of metal-encapsulated gold nanoclusters $M@Au_{12}$ (M = W, Mo) with I_h or O_h symmetry, and their structural and electronic properties. To determine the most stable dimer structure in each case, various configurations are considered. We find that during dimerization, gold atoms near the interface tend to form inter-cluster triangular bonds, which stabilize two monomer clusters by about 3.3–3.5 eV. The dimerization along a specific axis selected as the *z* axis causes the symmetry reduction of each $M@Au_{12}$ cluster resulting in the modification of electronic structures. It is found that all the stable dimers exhibit a much smaller HOMO–LUMO gap than those of their comprising monomers. Such a gap decrease is mainly attributed to the d_{z^2} orbital splitting of the central atoms owing to dimerization. We also calculate the vibrational modes and the corresponding IR-active spectra, which are distinguishable for different dimer configurations. In addition, we find that the IR-active modes of the O_h-based dimer structures appear to be red-shifted in comparison to those of I_h-based ones. Thus, the IR spectra may be utilized experimentally to discriminate dimer configurations with different central metal atoms and/or dissimilar structural symmetries.

1. Introduction

Nanoclusters have become very attractive in science and technology, since not only do they have intriguing physical and chemical properties, but they are also expected to be the building blocks of cluster-assembled materials to be used in future nanotechnology.[1,2] For instance, during the last quarter of a century, various carbon nanoclusters based on C_{60} fullerenes have been reported.[3–8] C_{60} fullerenes form not only a bulk structure with face-centred cubic symmetry, but also a variety of nanostructures under high pressure or specific light conditions.[9–12] It was intriguingly observed that C_{60} molecules can be encapsulated into a carbon nanotube (CNT) to form a nanopeapod structure.[13–16] Even more interestingly, when the nanopeapod structures are heated to 1100 °C, the encapsulated buckyballs are dimerized and further fused into "peanut-shaped" or nanocapsule structures inside their host CNTs.[17–19]

Similar to carbon fullerene molecules, stable gold nanoclusters have received considerable attention of researchers in many fields. It has been reported that, because of the nanosize effect, they exhibit interesting optical, magnetic, and even catalytic properties[20–31] that are not seen with bulk crystalline gold. In 2002, a new form of stable gold clusters with icosahedral symmetry (I_h) were proposed by Pyykkö and colleagues.[32] The proposed gold cluster comprises twelve gold atoms with a transition metal atom enclosed at the centre to form $M@Au_{12}$ (M = W, Mo, Ta^+), and are stabilized by the aurophilic attractions, the relativistic effects, and the perfect 18-electron rule.[33–36] Especially, $W@Au_{12}$ and $Mo@Au_{12}$ with several different symmetries such as I_h, O_h, and D_{5h} were experimentally observed.[33,34,36]

Because of their structural similarity to C_{60}, $M@Au_{12}$ nanoclusters may also function as basic building units for constructing nanostructures fused through the dimerization and further polymerization process. The topic of such dimerization and polymerization is very important for identifying the growth pattern or characterizing the core structure of gold nanoclusters. Previous studies showed that small closed shell bimetallic magic clusters MAu_4 (M = Ti, Zr, and Hf) are strongly stabilized by dimerization.[37–40] Here, we propose dimerization of $M@Au_{12}$ (M = W, Mo) nanostructures with either I_h or O_h symmetry analogous to dimerization of fullerene molecules, based on the first-principles study. Unlike their fullerene counterparts, these gold clusters have different encapsulated metal atoms and dissimilar structural symmetries, and therefore our proposed dimers could be extended to various nanostructures. In addition, we investigate the infrared (IR) active vibrational modes of stable dimer configurations to further understand the structural distinctions.

2. Computational details

To investigate the geometrical and electronic structures of dimerized gold nanoclusters, we performed density functional

[a]*Department of Physics and Research Institue for Basic Sciences, Kyung Hee University, Seoul 130-701, Korea. E-mail: ykkwon@khu.ac.kr*

[b]*Department of Physics and Graphene Research Institute, Sejong University, Seoul 143-747, Korea. E-mail: gunnkim@sejong.ac.kr*

theory (DFT) calculations using the Vienna *Ab-initio* Simulation Package (VASP).[41,42] Projector augmented wave potentials[43] and the generalized gradient approximation (GGA)[44] with the Perdew–Burke–Ernzerhof (PBE) functional[45] were employed to describe the valence electrons and exchange-correlation (XC) energy, respectively. Moreover, since three elements (Au, W, and Mo) considered in this study are heavy, the scalar relativistic effect and the spin-orbit (SO) coupling were taken into account. The cutoff energy was 450 eV for the plane wave basis set. The energies were converged within 10^{-5} eV, and the geometrical relaxations were continued until the residual forces on all atoms became smaller than 0.02 eV Å^{-1}. A cubic supercell with an edge length of 15 Å was used.

To explore the IR-active vibrational spectra, we repeated our calculations using another DFT package, DMol^3, which can deal with isolated molecules without considering periodic supercell configurations by utilizing a localized orbital basis set.[46,47] We used GGA with the PBE XC functional, as in the calculations using VASP. Double numerical with polarization (DNP) and all-electron scalar relativistic potential[48] were adopted. The optimized configurations obtained using both packages were almost identical. The force constant matrix and the derivation of the electric dipole moment were calculated to obtain the IR-active modes and intensities of M@Au$_{12}$ and their dimers.[49,50] However, the SO effects on the electronic structures cannot be considered using the DMol^3 code. Therefore, we made use of the VASP package to obtain the optimized geometries and electronic structures, considering the SO effects, and then we calculated the vibrational modes with the DMol^3 for the geometries from VASP.

3. Results and discussion

3.1. Structural properties

As the first step, we performed geometrical relaxation to obtain the equilibrium structures of four different monomer units distinguished by enclosed metal elements and symmetries. Fig. 1 depicts the typical structures of optimized M@Au$_{12}$ (M = W or Mo) clusters with I_h and O_h symmetries. They are just different in the surface bonding and the ligand symmetry of the central atom. In both cases, the central M atom makes 12 equivalent radial bonds with the surface Au atoms. In addition to these radial bonds, the I_h M@Au$_{12}$ cluster has 30 identical surface Au–Au bonds, which are ~2.88 Å and ~5% longer than the radial M–Au bonds, forming an icosahedron. On the other hand, in the O_h M@Au$_{12}$ cluster, there are 36 equidistant bonds consisting of 12 radial M–Au bonds and 24 surface Au–Au bonds forming a cuboctahedron, which has 6 squares and 8 equilateral triangles. Our calculations show that the bonds in the latter cluster are ≤0.1 Å shorter than the surface bonds in the former one in good agreement with a previous study.[33]

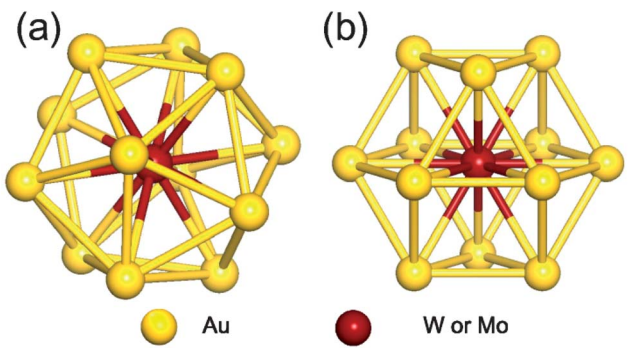

Fig. 1 Optimized structures of M@Au$_{12}$ (M = W, Mo) nanoclusters with (a) icosahedral (I_h) and (b) cuboctahedral (O_h) symmetries.

Based on the equilibrium structures, we evaluated the relative stability between I_h and O_h clusters and found that I_h M@Au$_{12}$ clusters are more stable than their O_h counterparts by ~0.18 eV and ~0.09 eV for M = W and Mo, respectively, consistent with a previous report.[33] However, I_h and O_h M@Au$_{12}$ clusters may coexist even at moderate temperature because their energy difference is quite small. To investigate the stability of dimer structures, we prepared more than 60 probable dimer configurations forming from any two monomer clusters to calculate their dimerization or formation energies, E_f defined by

$$E_f = E_{M_1@Au_{12}} + E_{M_2@Au_{12}} - E_{M_1@Au_{12}-M_2@Au_{12}}.$$

Here E_X is the total energy of an object X, which can be any monomer M_i@Au$_{12}$, (i = 1, 2) with either I_h or O_h symmetry, or M_1@Au$_{12}$–M_2@Au$_{12}$ dimer. The central metal atom M_i can be either W or Mo, depending on which the resulting dimer can be homogeneous ($M_1 = M_2$) or heterogeneous ($M_1 \neq M_2$). For given constituent monomers, we calculated formation energy values of various dimer configurations to determine the most stable one. Fig. 2 shows, among all cases taken into account, 7 selected dimer configurations: four configurations composed of I_h symmetric nanoclusters and three configurations for the O_h cluster.

The first four configurations displayed in Fig. 2(a)–(d) are denoted as follows: (a) I_h-A (A stands for "Atom") represents a dimer of two I_h monomers connected through a bond formed by two Au atoms from the respective monomers; (b) I_h–B (B for "Bond") connected by two parallel Au–Au bonds, each from each monomers; (c) I_h-BC (BC for "Bond Cross") combined through two perpendicular or crossed Au–Au bonds; and (d) I_h-FC (FC for "Face Cross") combined through two crossed triangular faces forming a hexagram in the axial view. The latter three dimer configurations shown in Fig. 2(e)–(g) are denoted by O_h-S (S for "Square"), O_h-SC (SC for "Square Cross"), and O_h-TC (TC for "Triangle Cross"), respectively: (e) O_h-S and (f) O_h-SC are dimers connected by two square faces, one from each O_h monomer, facing each other in parallel and with a relative rotation of 45° forming an octagram along the axial direction, respectively; and (g) O_h-TC combined by two crossed triangular faces forming a hexagram similar to I_h-FC. There are, of course, "hybrid" dimer configurations composed of I_h and O_h monomers, but our calculations show that initially-prepared hybrid dimers are transformed into "pure" dimers (I_h–I_h and O_h–O_h) after full relaxation. Therefore, here we do not present such hybrid dimer configurations.

The formation energy of each dimer configuration depends strongly on the bonding structures formed at the interface between two monomers. As indicated with the orange colour in

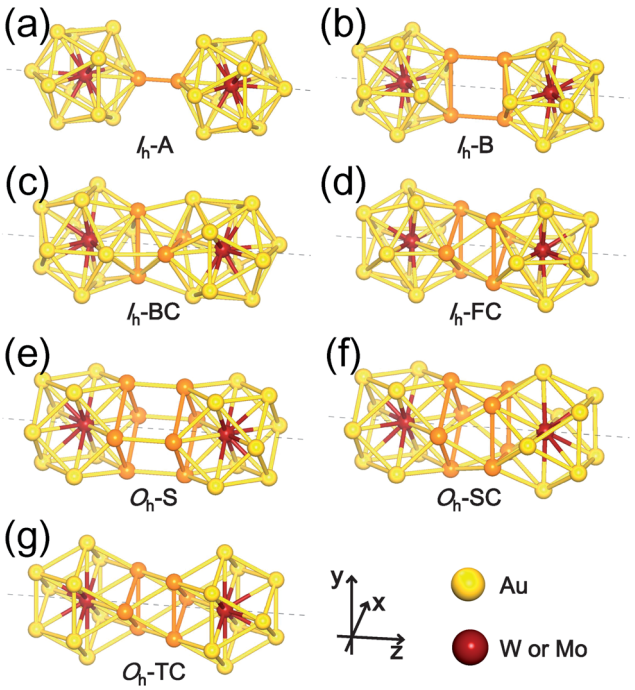

Fig. 2 Selected dimer configurations $M_1@Au_{12}$–$M_2@Au_{12}$: (a) I_h-A, (b) I_h-B, (c) I_h-BC, (d) I_h-FC, (e) O_h-S, (f) O_h-SC, and (g) O_h-TC. Au atoms participating in dimerization are represented by orange. The coordinates system used for dimerization is shown. See the text for the denotation of these dimer configurations.

Fig. 2, the bonding structure at the interface, which is evidently different from each other, is determined by the number of interacting Au atoms and their relative positions. Our calculations show that among the selected I_h-based dimer configurations, I_h-B is the least stable one due to the unfavourable bonding configuration. Even I_h-A, which has only a single bond connection between two participating monomers, is about 1 eV more stable.

The other two dimer configurations I_h-BC and I_h-FC are at least 2 eV more stable than the least stable one. We found that they have not only shorter inter-cluster distances, but also triangular bonding structures at their interfaces. Similarly, O_h-SC and O_h-TC, both of which have shorter inter-cluster distances and triangular bonding structures, are more stable than O_h-S. From these results, we conclude that the triangular bonding formation preferred by Au atoms enhances the dimer stability.

From now on, we will focus on these four (I_h-BC, I_h-FC, O_h-SC, and O_h-TC) stable dimer configurations. In Table 1, we summarized our results on the structural properties of the four stable dimer configurations including their formation energies, E_f, the distances between M_1 and M_2, $d_{M_1-M_2}$, as well as an average distances between M_i ($i = 1, 2$) and surface Au atoms, d_{M_i-Au}. For each dimer configuration, we considered two homogeneous (W–W and Mo–Mo) dimers and a heterogeneous W–Mo dimer. As is evident from Table 1, the Mo–Mo homogeneous dimer has the largest formation energy and the shortest M_1–M_2 distance for any given dimer configuration, but the formation energies of the other two dimer cases (W–W and W–Mo) are almost as large as the Mo–Mo dimer. It is also found that I_h-BC dimers are about 0.3 eV more stable than I_h-FC, so the former dimers would be abundant, whereas O_h-SC dimers are more stable than O_h-TC by 0.5–0.6 eV, so the former dimers are more likely to be observed. Nevertheless, we expect that various dimer configurations would form under different dimensional constraint.

3.2. Electronic properties

Any $M@Au_{12}$ monomer cluster with either I_h or O_h symmetry is highly symmetric. Hence dimerization of any two monomers may reduce their symmetries and thus modify their electronic properties. We found that such modification appears to occur mainly on the d states of the central metal atom and the s states of the surface Au atoms. It was also found that as long as the comprising monomer clusters keep their symmetries in their dimer configuration, the electronic structure modification remains similar regardless of two comprising central metal atoms. Therefore, in this section we describe the electronic structures of the most stable homogeneous W–W dimers, I_h-BC and O_h-SC, as well as those of their corresponding respective constituent $W@Au_{12}$ monomers.

3.2.1. $M@Au_{12}$ monomer clusters. To elucidate the electronic properties of the $M@Au_{12}$ clusters, we calculated the projected density of states (PDOS) onto the 6s and each of five 5d orbitals (d_{z^2}, $d_{x^2-y^2}$, d_{xy}, d_{yz}, and d_{zx}) of the metal impurity as well as some of the surface Au_{12} corresponding to those locating near the interface of the dimer configuration. Fig. 3(a) and 4(a) present the calculated PDOS as well as the total DOS for the I_h and O_h $W@Au_{12}$ clusters, respectively, without the SO coupling, while Fig. 3(b) and 4(b) show those with the SO coupling.

Table 1 The formation energies E_f, centre-to-centre distances $d_{M_1-M_2}$, centre-to-surface distances d_{M_i-Au}, and HOMO–LUMO energy gap, E_{gap} of the dimers with various compositions and the chosen dimer configurations: I_h-BC, I_h-FC, O_h-SC, and O_h-TC. For each dimer configuration, there are two kinds of homogeneous dimers (W–W, Mo–Mo) and one heterogeneous dimer (W–Mo)

Configurations	I_h-BC			I_h-FC			O_h-SC			O_h-TC		
M_1–M_2	W–W	Mo–Mo	W–Mo	W–W	Mo–Mo	W–Mo	W–W	Mo–Mo	W–Mo	W–W	Mo–Mo	W–Mo
E_f (eV)	3.364	3.481	3.422	3.048	3.214	3.114	3.354	3.472	3.403	2.843	2.857	2.845
$d_{M_1-M_2}$ (Å)	6.467	6.398	6.433	6.500	6.334	6.473	6.475	6.433	6.458	6.826	6.820	6.819
d_{M_1-Au} (Å)	2.754	2.760	2.753	2.753	2.761	2.753	2.806	2.811	2.806	2.797	2.804	2.798
d_{M_2-Au} (Å)	2.754	2.760	2.758	2.753	2.761	2.759	2.805	2.811	2.812	2.797	2.804	2.805
E_{gap} (eV)	0.812	0.732	0.757	0.497	0.404	0.459	0.440	0.385	0.401	0.659	0.564	0.594

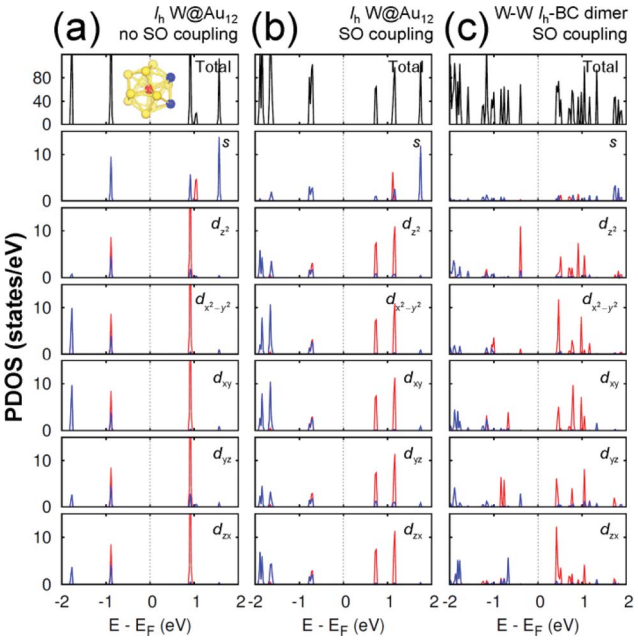

Fig. 3 The PDOS of I_h W@Au_{12} cluster without the SO coupling effect (a), with the SO coupling effect (b), and of I_h-BC dimer (c). In the PDOS for each orbital, the red (blue) line is used for the W atom (Au atoms), which is (are) marked with the same colour in the inset of (a). The same coordinates system is used as shown in Fig. 2.

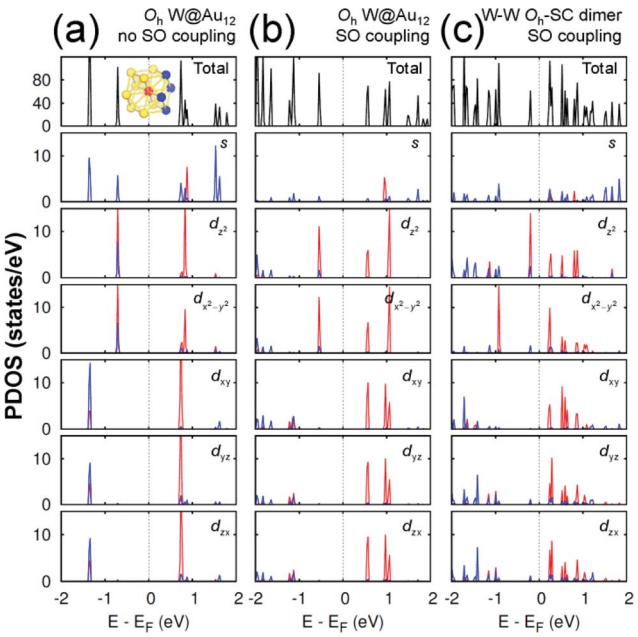

Fig. 4 The PDOS of O_h W@Au_{12} cluster without the SO coupling effect (a), with the SO coupling effect (b), and of O_h-SC dimer (c). In the PDOS for each orbital, the red (blue) line is used for the W atom (Au atoms), which is (are) marked with the same colour in the inset of (a). The same coordinates system is used as shown in Fig. 2.

In an I_h W@Au_{12} cluster, its twelve 6s orbitals of Au_{12} span the irreducible representations of $a_g + t_{1u} + h_g + t_{2u}$. At the same time, the first three representations are spanned respectively by the s, p, and d atomic orbitals of the central atom.[32] As a result, the major orbital interactions in W@Au_{12} occur mainly between Au_{12} ligand group orbitals and the 5d orbitals of the W atom resulting in the highest occupied molecular orbital (HOMO) with the bonding h_g and the lowest unoccupied molecular orbital (LUMO) with the antibonding h_g^*.

As shown in Fig. 3(a), the HOMO level of I_h W@Au_{12} is composed of the degenerate 5d orbitals of the central W atom and 6s and 5d orbitals of the surface Au atoms, while its LUMO level is mainly comprised of the degenerate 5d orbitals of the W atom. The SO coupling splits each 5d state of the W atom at the LUMO level significantly into two states separated by ~0.44 eV, whereas its counter state at the HOMO splits only by ~0.03 eV as shown in Fig. 3(b). It is also shown in Fig. 3(b) that the occupied states of the surface gold atoms, which have been located quite below the HOMO level without SO coupling, tend to shift towards the HOMO level due to the SO splitting. Some of the results are in close agreement with a previous report.[33]

On the other hand, the O_h W@Au_{12} cluster is affected by the crystal field effect of the O_h ligand on the central metal atom W. The 5d orbitals of the central atom, which have been degenerate in the I_h cluster, are split into two distinct states. One is the higher energy state of e_g comprising d_{z^2} and $d_{x^2-y^2}$, and the other is the lower energy state of t_{2g} composed of d_{xy}, d_{yz}, and d_{zx} as seen in Fig. 4(a). As a result, the e_g state becomes the HOMO level of the O_h cluster. To the empty molecular orbitals, in contrast, such a crystal field effect appears less significant resulting in small splitting, and the t_{2g}^* state becomes the LUMO level.

As shown in Fig. 4(b), the SO coupling effect on the O_h cluster is similar to on the I_h one: further splitting of the occupied and unoccupied molecular orbitals by about 0.01 and 0.4 eV, respectively. These two effects of the level splitting reduce the HOMO–LUMO energy gap of the O_h cluster to $E_{gap} \approx 1.115$ eV compared to $E_{gap} \approx 1.437$ eV of the I_h cluster. Similar tendencies were found for Mo@Au_{12} clusters with both I_h and O_h Mo@Au_{12} symmetries. Their respective energy gaps were calculated to be 1.343 eV and 1.088 eV.

3.2.2. M_1@Au_{12}–M_2@Au_{12} dimers. To investigate the effect of dimerization on the electronic properties of these highly symmetric M@Au_{12} clusters, we calculated, with the SO coupling on, the PDOS of the most stable homogeneous W–W dimers, I_h-BC and O_h-SC, as well as their total DOS. The calculated PDOS of the respective dimers are displayed in Fig. 3(c) and 4(c). It is shown that most molecular levels appeared in Fig. 3(b) and 4(b) are split further into many states, as shown in Fig. 3(c) and 4(c), owing to the symmetry breaking caused by dimerization.

Since the z axis was selected as the dimerization axis, we found in both I_h-BC and O_h-SC that the most remarkable changes take place at the occupied d_{z^2} orbital. The symmetry breaking due to dimerization pushes up the occupied d_{z^2} of the central W atom close to the Fermi level being the HOMO of each dimer. The W HOMO level of I_h-BC appears to be hybridized with Au d_{yz} as shown in Fig. 3(c), which is contributed from two Au atoms coloured in blue shown in the inset of Fig. 3(a). In contrast for O_h-SC as shown in Fig. 4(c), the W HOMO level

seems to interact weakly with Au $d_{x^2-y^2}$, d_{yz}, and d_{zx}, which are from those four Au atoms marked in blue in the inset of Fig. 4(a). For both dimers, the $d_{x^2-y^2}$ orbital split much less, because dimerization left this orbital still intact. The unoccupied states are mainly comprised of W 5d orbitals, which are split into many states resulting in the lowest level of each d orbital pushed down toward the Fermi level.

As a result, dimerization gives rise to a significant decrease in E_{gap}, as shown in Fig. 3(c) and 4(c). Such a significant reduction in E_{gap} was observed in all dimer configurations, not only I_h-BC and O_h-SC described above, but also I_h-FC and O_h-TC, with any combinations of central metal atoms (W–W, Mo–Mo, or W–Mo). We further found that the dimer configurations with the same symmetry have similar E_{gap} values within less than 0.1 eV difference, regardless of the central metal compositions. We also observed another trend independent of dimer symmetries. For each given dimer configuration, the W–W dimer has the largest E_{gap}; the Mo–Mo dimer has the smallest; and E_{gap} of the W–Mo heterogeneous dimer is in between, as listed in Table 1. All dimer configurations reveal different E_{gap} from one another, and smaller gap than their respective monomer clusters. Among all these dimers, the O_h-SC dimer reveals the smallest E_{gap}. Due to such difference and reduction in E_{gap}, the electronic property of each dimer may be different from each other, and distinguishable from the monomers. Our study will be extended further to investigate the electronic structures of $M@Au_{12}$ based nanowires.

3.3. IR spectra

To further understand the structural distinctions, we investigated the IR-active spectra for various dimer configurations. The vibrational modes were calculated from the force constant matrix obtained by displacing each atom in the cluster in all directions. Fig. 5(a) and (b) show the calculated IR-active modes of the dimers $M_1@Au_{12}$–$M_2@Au_{12}$ (M_i = W, Mo) with I_h and O_h symmetries, respectively, as well as of respective corresponding clusters for comparison. Due to different atomic mass of W and Mo, $W@Au_{12}$ and $Mo@Au_{12}$ clusters show IR peaks at different frequencies. In Fig. 5(a), the intense IR peaks at 201–204 cm^{-1} for I_h $W@Au_{12}$ and 254–256 cm^{-1} for I_h $Mo@Au_{12}$ represent the vibrational modes of the central atoms, whereas those at 178 cm^{-1} and 226 cm^{-1} in Fig. 5(b) correspond to those of the O_h clusters. It is obvious that the IR-active modes of the central metal atoms of the O_h clusters are red-shifted, as compared with those of the I_h clusters. This red-shift is attributed to shallow interaction in the O_h cluster due to its longer M–Au bond length than that of the I_h cluster. It is clear that the vibrational frequency, ν, is inversely proportional to $\sqrt{m}$, that is,

$$\sqrt{\frac{m_W}{m_{Mo}}} \approx \sqrt{\frac{184}{96}} \approx \frac{255}{202} \approx \frac{226}{178} = \frac{\nu_{Mo}}{\nu_W},$$

where m_W ($\approx$184) and m_{Mo} ($\approx$96) are atomic masses of W and Mo. Other IR-active vibrational modes of the surface Au atoms, forming a spherical cage structure, were found near ~100 cm^{-1} in both cases of I_h and O_h clusters. For the O_h $M@Au_{12}$ clusters, there were also low intensity peaks at ~70 cm^{-1} and ~86 cm^{-1} corresponding to other vibrational modes of the central metal atom and the surface Au atoms. Since the vibrational modes of the M atom were separate from those of Au atoms and distinguishable between the W and Mo atoms, we expect that the dimers with different configurations and compositions could be identified using IR spectra.

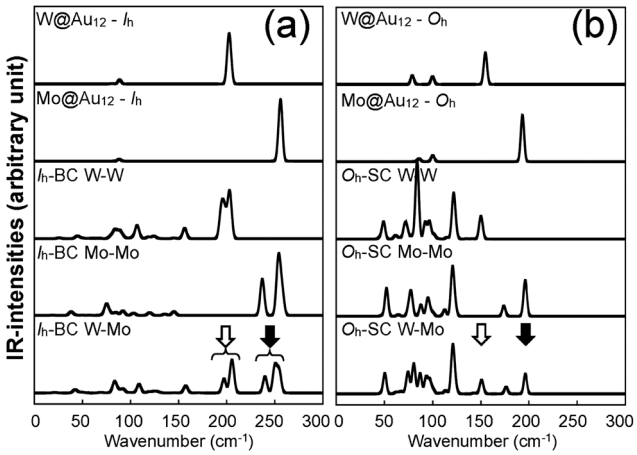

Fig. 5 IR spectra of (a) I_h monomers and I_h-BC dimers and (b) O_h monomers and O_h-SC dimers. From top to bottom, $W@Au_{12}$ and $Mo@Au_{12}$ monomers (top two panels), and the most stable dimer configurations with the central metal composition of W–W (3rd panel), Mo–Mo (4th panel), and W–Mo (5th panel) with (a) I_h and (b) O_h symmetries. The empty arrows indicate the vibration frequencies of W atoms in each dimer while the filled arrows indicate those of Mo atoms.

For the homogeneous M–M I_h-BC dimer, the intense peaks at 198–203 cm^{-1} and 253–257 cm^{-1} appearing for M = W and Mo, respectively, correspond to the vibrational modes of the central atom along the x and y axes; the intense peaks at 194 cm^{-1} and 237 cm^{-1} in Fig. 5(a) correspond to those along the z axis with in-phase modes.

The vectors of these separate and in-phase modes of the W and Mo atoms are presented in Fig. 6(a) and they clearly show the direction of the vibrations at given frequencies. Moreover, because the symmetry is broken owing to dimerization, the vibrational modes of the Au atoms split into various modes including in-plane stretching modes, radial modes for each cluster, and stretching modes of the bonds between two clusters. Among these various modes from the Au atoms, we present the vector of the in-plane stretching modes in Fig. 6(a).

For the heterogeneous W–Mo I_h-BC dimer, the IR spectrum (Fig. 5(a), bottom) shows intense peaks at 197–206 cm^{-1} and 239–254 cm^{-1} corresponding to the vibrations along the x, y, and z axes of the central W and Mo atoms, respectively. Their corresponding vector representations are shown in Fig. 6(b). The modes of the surface Au atoms are still active at almost the same frequency as those of the homogeneous dimers. Interestingly, the in-phase vibrational modes of the W and Mo atoms along the z axis disappeared while the separate modes at a similar frequency to those of homogeneous W–W and Mo–Mo I_h-BC.

We also performed the same calculations for O_h-SC dimers. The IR-active spectra and the vector representation of modes are presented in Fig. 5(b) and 6(c)–(d), respectively. The IR spectra are different from those of I_h-BC because of the different

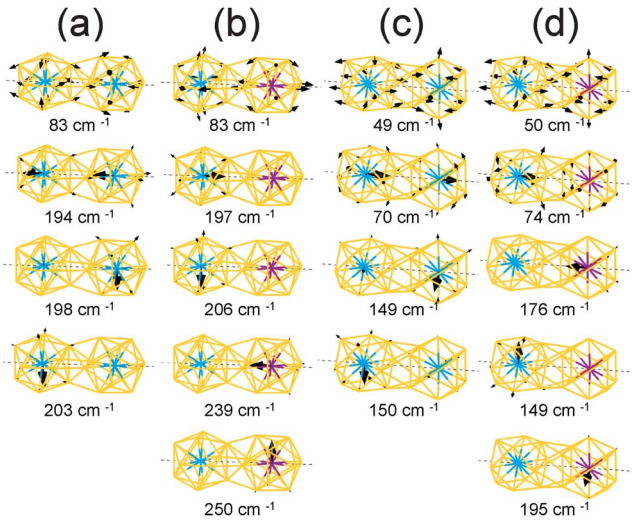

Fig. 6 The vector representation of IR-active vibrational modes of homogeneous (W–W) and heterogeneous (W–Mo) dimers with I_h-BC (a and b) and O_h-SC (c and d) configurations. For all dimer configurations, homogeneous dimers have in-phase vibration modes of metal impurities at the centre of the clusters, whereas such modes disappeared in the cases of the heterogeneous dimers.

symmetries. It turned out that the vibrational modes of the Au atoms are more intense than their monomer counterparts. This may be due to mixing of the vibrational modes of the central atom and the surface Au atoms in the O_h clusters, as mentioned above. The intense peaks at ~150 cm^{-1} and 195–197 cm^{-1} correspond to the vibrational modes of the central atom in the *xy*-plane, which becomes clear in the vector representation at given frequencies in Fig. 6(c).

We found the drastic difference in the frequency and behaviour of in-phase mode of the two W atoms along the *z* axis. This mode appeared at much lower frequency ~70 cm^{-1}, as shown in the 3rd graph of Fig. 5(b) and also in the vector representation of Fig. 6(c), than in W–W I_h-BC. However, the overall tendency of changes in the IR spectra owing to the different central atoms is practically the same as for I_h dimers. Similar to that of I_h-BC dimer, the heterogeneous W–Mo O_h-SC exhibits the vibrational modes of the Au atoms, and the W and Mo atoms at nearly the same frequencies as in two homogeneous O_h-SC dimers. From our investigation of IR spectra, we propose that the symmetries, configurations, and impurity compositions of various M_1Au_{12}–M_2Au_{12} dimers can be identified through the IR spectroscopy experiment.

4. Conclusions

Using density functional theory, we studied the dimerization of metal-encapsulated Au_{12} nanoclusters ($M@Au_{12}$, M = W, Mo) with either I_h or O_h symmetry. The most stable dimer structure in each case was determined among a variety of candidate dimer configurations. It was found that Au atoms from one monomer cluster located near the interface tend to form extra triangular bonds with Au atoms nearby from the other cluster during dimerization, which stabilizes the monomer clusters by about 3.3–3.5 eV. The dimerization along a specific axis selected as the *z* axis causes the symmetry reduction of each $M@Au_{12}$ cluster resulting in the modification of electronic structures. We found that all the stable dimers exhibit much smaller HOMO–LUMO gap E_{gap} mainly determined by the d_{z^2} orbitals of the central atoms split owing to dimerization than those of their comprising monomers. We also investigated the vibrational modes and IR-active spectra for various dimers. The IR-active spectra were calculated to be significantly varied for different dimer configurations. In addition, we found that the IR-active modes of the O_h-based dimer structures appear to be red-shifted in comparison to those of I_h-based ones. Thus the IR spectra may be utilized experimentally to distinguish dimer configurations with different central metal atoms and/or different structural symmetries.

Acknowledgements

We gratefully acknowledge financial support from the Korean government through National Research Foundation (NRF-2011-0016188, 2010-0020207 and 2013R1A1A2009131). Some portion of our computational work was done using the resources of the KISTI Supercomputing Center (KSC-2012-C2-72 and KSC-2013-C2-024).

References

1 S. A. Claridge, A. W. Castleman, Jr, S. N. Khanna, C. B. Murray, A. Sen and P. S. Weiss, *ACS Nano*, 2009, **3**, 244.
2 M. Qian, A. C. Reber, A. Ugrinov, N. K. Chaki, S. Mandal, H. M. Saavedra, S. N. Khanna, A. Sen and P. S. Weiss, *ACS Nano*, 2010, **4**, 235.
3 H. W. Kroto, J. R. Heath, S. C. O'Brien, R. F. Curl and R. E. Smalley, *Nature*, 1985, **318**, 162.
4 W. Kratschmer, L. D. Lamb, K. Fostiropoulos and D. R. Huffman, *Nature*, 1990, **347**, 354.
5 M. S. Dresselhaus and G. Dresselhaus, *Nanostruct. Mater.*, 1997, **9**, 33.
6 A. M. Cassell, C. L. Asplund and J. M. Tour, *Angew. Chem., Int. Ed.*, 1999, **38**, 2403.
7 H. Hirai, K. Kondo, N. Yoshizawa and M. Shiraishi, *Appl. Phys. Lett.*, 1994, **64**, 1797.
8 M. Prato, *J. Mater. Chem.*, 1997, **7**, 1097.
9 A. M. Rao, P. C. Eklund, J. L. Hodeau, L. Marques and M. Nunez-Regueiro, *Phys. Rev. B: Condens. Matter Mater. Phys.*, 1997, **55**, 4766.
10 A. Takashima, J. Onoe and T. Nishii, *J. Appl. Phys.*, 2010, **108**, 033514.
11 K. P. Meletov, S. Assimopoulos, I. Tsilika, G. A. Kourouklis, J. Arvanitidis, S. Ves, B. Sundqvist and T. Wagberg, *Chem. Phys. Lett.*, 2001, **341**, 435.
12 V. D. Blank, S. G. Buga, N. R. Serebryanaya, V. N. Denisov, G. A. Dubitsky, A. N. Ivlev, B. N. Mavrin and M. Y. Popov, *Phys. Lett. A*, 1995, **205**, 208.
13 B. W. Smith, M. Monthioux and D. E. Luzzi, *Nature*, 1998, **396**, 323.
14 B. W. Smith, M. Monthioux and D. E. Luzzi, *Chem. Phys. Lett.*, 1999, **315**, 31.

15 S. Berber, Y.-K. Kwon and D. Tománek, *Phys. Rev. Lett.*, 2002, **88**, 185502.
16 Y. Cho, S. Han, G. Kim, H. Lee and J. Ihm, *Phys. Rev. Lett.*, 2003, **90**, 106402.
17 B. W. Smith and D. E. Luzzi, *Chem. Phys. Lett.*, 2000, **321**, 169.
18 S. Bandow, M. Takizawa, K. Hirahara, M. Yudasaka and S. Iijima, *Chem. Phys. Lett.*, 2001, **337**, 48.
19 S. Han, M. Yoon, S. Berber, N. Park, E. Osawa, J. Ihm and D. Tománek, *Phys. Rev. B: Condens. Matter Mater. Phys.*, 2004, **70**, 113402.
20 M. Brust, J. Fink, D. Bethell, D. J. Schiffrin and C. Kiely, *J. Chem. Soc., Chem. Commun.*, 1995, 1655.
21 A. Sanchez, S. Abbet, U. Heiz, W. D. Schneider, H. Hakkinen, R. N. Barnett and U. Landman, *J. Phys. Chem. A*, 1999, **103**, 9573.
22 P. Schwerdtfeger, *Angew. Chem., Int. Ed.*, 2003, **42**, 1892.
23 J. Zhao, J. Yang and J. G. Hou, *Phys. Rev. B: Condens. Matter Mater. Phys.*, 2003, **67**, 085404.
24 M.-C. Daniel and D. Astruc, *Chem. Rev.*, 2003, **104**, 293.
25 M. Turner, V. B. Golovko, O. P. H. Vaughan, P. Abdulkin, A. Berenguer-Murcia, M. S. Tikhov, B. F. G. Johnson and R. M. Lambert, *Nature*, 2008, **454**, 981.
26 B. Palpant, B. Prével, J. Lermé, E. Cottancin, M. Pellarin, M. Treilleux, A. Perez, J. L. Vialle and M. Broyer, *Phys. Rev. B: Condens. Matter Mater. Phys.*, 1998, **57**, 1963.
27 N. Lopez and J. K. Norskov, *J. Am. Chem. Soc.*, 2002, **124**, 11262.
28 T. V. Choudhary and D. W. Goodman, *Top. Catal.*, 2002, **21**, 25.
29 Y. Yamamoto, T. Miura, M. Suzuki, N. Kawamura, H. Miyagawa, T. Nakamura, K. Kobayashi, T. Teranishi and H. Hori, *Phys. Rev. Lett.*, 2004, **93**, 116801.
30 G. Kim, S.-H. Kang, C.-Y. Lim and Y.-K. Kwon, *Chem. Phys. Lett.*, 2012, **545**, 83.
31 S.-H. Kang, G. Kim and Y.-K. Kwon, *J. Phys.: Condens. Matter*, 2011, **23**, 505301.
32 P. Pyykkö and N. Runeberg, *Angew. Chem.*, 2002, **114**, 2278.
33 X. Li, B. Kiran, J. Li, H. J. Zhai and L. S. Wang, *Angew. Chem., Int. Ed.*, 2002, **41**, 4786.
34 J. Long, Y.-X. Qiu, X.-Y. Chen and S.-G. Wang, *J. Phys. Chem. C*, 2008, **112**, 12646.
35 P. Pyykkö, *J. Organomet. Chem.*, 2006, **691**, 4336.
36 Y.-X. Qiu, S.-G. Wang and W. H. E. Schwarz, *Chem. Phys. Lett.*, 2004, **397**, 374.
37 Y.-K. Han, J. C. Kim, J. Jung and U. Yu, *Bull. Korean Chem. Soc.*, 2008, **29**, 305.
38 M.-X. Chen and X. H. Yan, *J. Chem. Phys.*, 2008, **128**, 174305.
39 T. K. Ghanty, K. R. S. Chandrakumar and S. K. Ghosh, *J. Chem. Phys.*, 2004, **120**, 11363.
40 J. Jung, H. Kim, J. C. Kim, M. H. Park and Y.-K. Han, *Chem.–Asian J.*, 2011, **6**, 868.
41 G. Kresse and J. Furthmüller, *Phys. Rev. B: Condens. Matter Mater. Phys.*, 1996, **54**, 11169.
42 G. Kresse and J. Furthmüller, *Comput. Mater. Sci.*, 1996, **6**, 15.
43 P. E. Blöchl, *Phys. Rev. B: Condens. Matter Mater. Phys.*, 1994, **50**, 17953.
44 J. P. Perdew and W. Yue, *Phys. Rev. B: Condens. Matter Mater. Phys.*, 1986, **33**, 8800.
45 J. P. Perdew, K. Burke and M. Ernzerhof, *Phys. Rev. Lett.*, 1996, **77**, 3865.
46 B. Delley, *J. Chem. Phys.*, 2000, **113**, 7756.
47 B. Delley, *J. Chem. Phys.*, 1990, **92**, 508.
48 D. D. Koelling and B. N. Harmon, *J. Phys. C: Solid State Phys.*, 1977, **10**, 3107.
49 G. Herzberg and B. L. Crawford, *J. Phys. Chem.*, 1946, **50**, 288.
50 J. E. B. Wilson, J. G. Decius, P. G. Cross and R. T. Lagemann, *Am. J. Phys.*, 1955, **23**, 550.

